Universiteit Antwerpen

This item is the archived peer-reviewed author-version of:

Structure-property relations of methylamine vapor treated hybrid perovskite $CH_3NH_3PbI_3$ films and solar cells

Structure-Property Relations of Methylamine Vapor Treated Hybrid Perovskite CH₃NH₃PbI₃ Films and Solar Cells

Bert Conings[1,2]*, Simon A. Bretschneider[3], Aslihan Babayigit[1,2], Nicolas Gauquelin[4], Ilaria Cardinaletti[1], Jean Manca[5], Jo Verbeeck[4], Henry J. Snaith[2], Hans-Gerd Boyen[1]

[1]Hasselt University, Institute for Materials Research (IMO), Wetenschapspark 1, 3590 Diepenbeek, Belgium.

[2]University of Oxford, Department of Physics, Clarendon Laboratory, Parks Road, Oxford OX1 3PU, UK.

[3]Max Planck Institute for Polymer Research - Molecular Spectroscopy Group, Ackermannweg 10, 55128 Mainz, Germany.

[4]University of Antwerp, Electron Microscopy for Materials Research, University of Antwerp, Groenenborgerlaan 171, 2020, Antwerp, Belgium.

[5]Hasselt University, X-Lab, Agoralaan 1, Building D, 3590, Diepenbeek, Belgium.

*bert.conings@uhasselt.be

Abstract

The power conversion efficiency of halide perovskite solar cells is heavily dependent on the perovskite layer being sufficiently smooth and pinhole-free. It has been shown that these features can be obtained even when starting out from rough and discontinuous perovskite film, by briefly exposing it to methylamine (MA) vapor. The exact underlying physical mechanisms of this phenomenon are, however, still unclear. By investigating smooth, MA treated films, based on very rough and discontinuous reference films of methylammonium triiode (MAPbI$_3$), considering their morphology, crystalline features, local conductive properties, and charge carrier lifetime, we unravel the relation between their characteristic physical qualities and their performance in corresponding solar cells. We discover that the extensive improvement in photovoltaic performance upon MA treatment is a consequence of the induced morphological enhancement of the perovskite layer, together with improved electron injection into TiO$_2$, which in fact compensates for an otherwise compromised bulk electronic quality, simultaneously caused by the MA treatment.

Introduction

Hybrid metal halide perovskite solar cells have dramatically altered the landscape of photovoltaics (PV) in the last few years.[1-3] These perovskite light absorbers royally outclass the typical competing state-of-the-art organic and dye-sensitized PV materials in several critical physical properties and, by extension, performance. Another main selling point of perovskites is their cost-effective fabrication potential— the required chemicals are very inexpensive and perovskites can be deposited via solution processing at low temperatures, allowing them to be mass-produced by means of established coating techniques such as doctor blading, slot-die coating or spray coating.[4-6] With this in mind, many researchers in the field have worked out dedicated methods to increase film quality, both morphologically and related to charge carrier transport properties.[7-8] These include a multitude of post-processing strategies, including thermal annealing,[9-10] solvent annealing,[11-12] or a combination of those,[13] optionally under different atmospheres,[14] and treatment with ammonium salts.[15-17] Arguably the most disruptive one was introduced by Z. Zhou et al., where any rough and discontinuous $MAPbI_3$ film—that typically yields a bad solar cell, can be transformed into a smooth high-quality film that yields considerably superior performance.[18] In this approach, the defective $MAPbI_3$ film is exposed to methylamine (MA) gas, bringing the former into a liquefied state and thereby evening it out, all in a matter of seconds. Upon removal of the residual MA, the film recrystallizes and becomes smooth and pinhole-free. The reversibility of this process hinges on the commonality of the methyl group in $MAPbI_3$ and MA, as Zhou et al. demonstrated. More recently, Y. Zhou et al. extended the applicability of gas treatment to low-quality formamidinium lead triiode ($FAPbI_3$) films, which in turn can be recrystallized into high quality films after exposure to formamidine gas at 150°C.[19] The main potential of these gas treatments lies in their use in up-scaled fabrication of perovskite films: As it is generally considered a challenge to produce large-area perovskite films of uniformly high quality by means of typical coating techniques (except vacuum processing)[20-21], the more convenient alternative approach would be to loosen the requirements for freshly coated films and post-treat them with the appropriate gas to obtain high quality films after all. In a related account, Raga et al. demonstrated that direct MA-exposure of pure PbI_2 can even lead to high quality $MAPbI_3$ perovskite, provided the presence of HI gas.[22] Jiang *et al*. and Jacobs et al. independently discovered that heating the substrate during gas treatment allows to obtain films with larger grains and lower defect densities.[23-24] The physicochemical events occurring during the gas treatment, and how these are affected by parameters such as interaction time and pressure, were reported by Zhao *et al*.[25] In the current work, we investigate the structure-property relations for pristine and MA treated films and corresponding solar cells, to pinpoint the exact relation between their characteristic physical features and their photovoltaic performance. We fabricated perovskite films and solar cells of the architecture tin-doped indium oxide (ITO)/compact TiO_2/mesoporous TiO_2/perovskite/spiro-OMeTAD/Au, where the perovskite was treated with MA vapor. The morphology of these films and complete solar cells was investigated with Scanning Electron Microscopy (SEM) and High-Angle Annular Dark Field Scanning Transmission Electron Microscopy (HAADF-STEM). The observed structural features were correlated to local currents by

means of Conductive Atomic Force Microscopy (C-AFM), and the decay of the photo-induced processes in pristine and treated films were measured by Time-Resolved PhotoLuminescence (TRPL).

Results and discussion

Figure 1a and b show Scanning Electron Microscopy (SEM) images of the perovskite layers we obtain via spin coating of the classic PbI_2:MAI precursor (1:1 molar ratio in DMF), followed by heating at 100°C for 10 minutes. The films are discontinuous, showing the underlying mesoporous TiO_2, and exhibit large dendritic structures, very much like what has been reported by many others, and therefore a reliable point of reference.[18, 26-27] For the MA treatment of these films, we adapted a procedure from Zhao et al.,[25] using off-the-shelf MA solution in ethanol. The treated films (shown in Figure 1c and d) are smooth and pinhole-free, indicating that the treatment is successful. The X-Ray Diffraction (XRD) data in Figure 1e indeed show that the count rate for a treated film is significantly higher than for a pristine film, proving that the former is more crystalline, and confirming the pioneering work of Z. Zhou *et al.*[18]
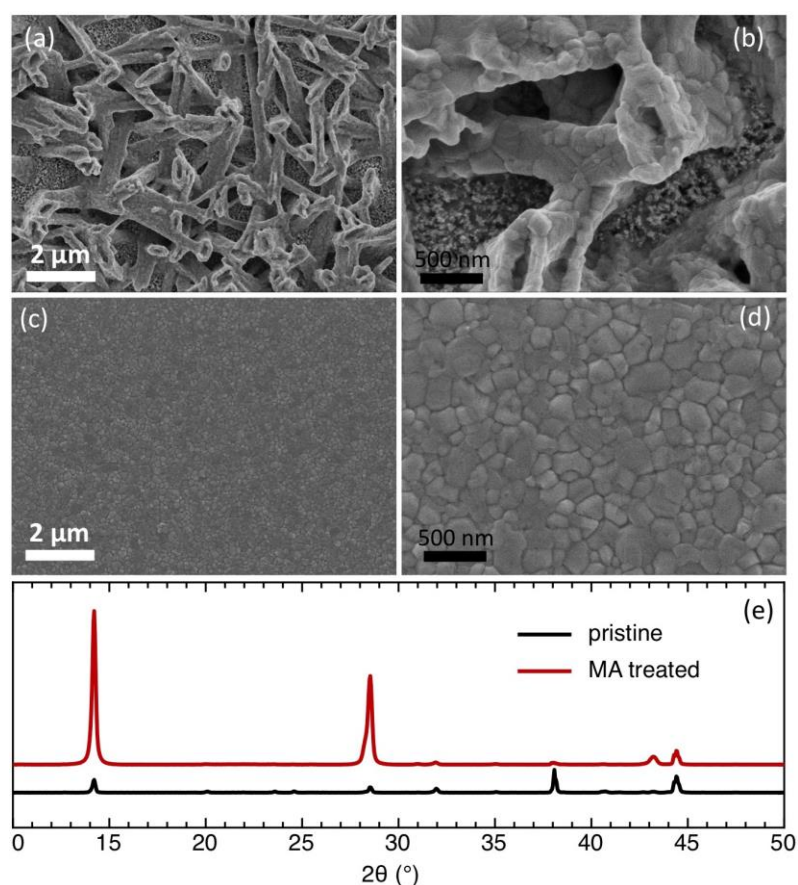

Figure 1: SEM images of MAPbI₃ layers at two magnifications. (a) and (b): pristine layers; (c) and (d): MA treated layers. (e) XRD data of both pristine and MA treated samples.

Solar cells were then fabricated based on the pristine and MA treated MAPbI$_3$ films, using the mesoporous TiO$_2$ device embodiment. The corresponding photovoltaic parameters are listed in Table 1. As expected based on the rough topography and in keeping with existing literature, the solar cells based on pristine films exhibit quite low performance, averaging 8.3 % on the backward current density-voltage (JV) scan. These are significantly outperformed by their MA treated counterparts, which show a vast improvement in short circuit current (J$_{sc}$), open-circuit voltage (V$_{oc}$) and fill factor (FF), resulting in an overall average efficiency of 16.6%, with a maximum obtained value of 17.5%. Forward and reverse JV curves of the best devices (Figure S1a) show a palpable degree of hysteresis, commonly observed in perovskite solar cells.[28-29] The stabilized power output (SPO, See Figure S1b) is therefore a better measure for their performance, adding up to an average of 6.0% for the pristine cells, and 16.2% for the treated cells (with a maximum of 16.9%). These values are higher than those reported by Z. Zhou et al. and Raga et al., who use the same device architecture.[18, 22]

Table 1: Photovoltaic performance of solar cells with pristine and MA treated perovskite layers. The values represent averages and standard deviations of reverse scans of 16 devices for each condition (or 4 devices for SPO). Maximum obtained values are given between brackets.

	J_{sc} (mA·cm^{-2})	V_{oc} (V)	FF (-)	PCE (%)	SPO (%)
pristine	17.2 ± 0.7	0.903 ± 0.013	0.532 ± 0.013	8.30 ± 0.54	6.0 ± 0.3
	[18.4]	[0.915]	[0.543]	[9.08]	[6.2]
MA	21.8 ± 0.6	1.07 ± 0.013	0.707 ± 0.010	16.6 ± 0.5	16.2 ± 0.6
treated	[23.2]	[1.09]	[0.730]	[17.5]	[16.9]

Now that we have demonstrated representative baseline pristine solar cells and confirmed the effectiveness of our adapted approach for MA treatment, we turn to a more exhaustive examination in an effort to ascertain which is the main reason for the improvement in device performance upon MA treatment. Z. Zhou suggests that the liquefaction of the perovskite upon MA treatment would assist in its infiltration into the mesoporous TiO$_2$ scaffold. It is also suggested that the removal of macroscopic film defects is the principal reason for this improvement in performance[18, 25] (and Z. Zhou et al. even term the treatment "gas induced defect healing")[18] but there is still a lack of hard evidence to support this hypothesis. Notably, the complete loss of crystal structure of the perovskite film upon MA exposure—and subsequent recrystallization—does suggest that the treatment is much more radical than a mere curing of defects, and thus indicates the need for further investigation. As such, we started out by studying cross-sections of complete solar cells using HAADF-STEM.
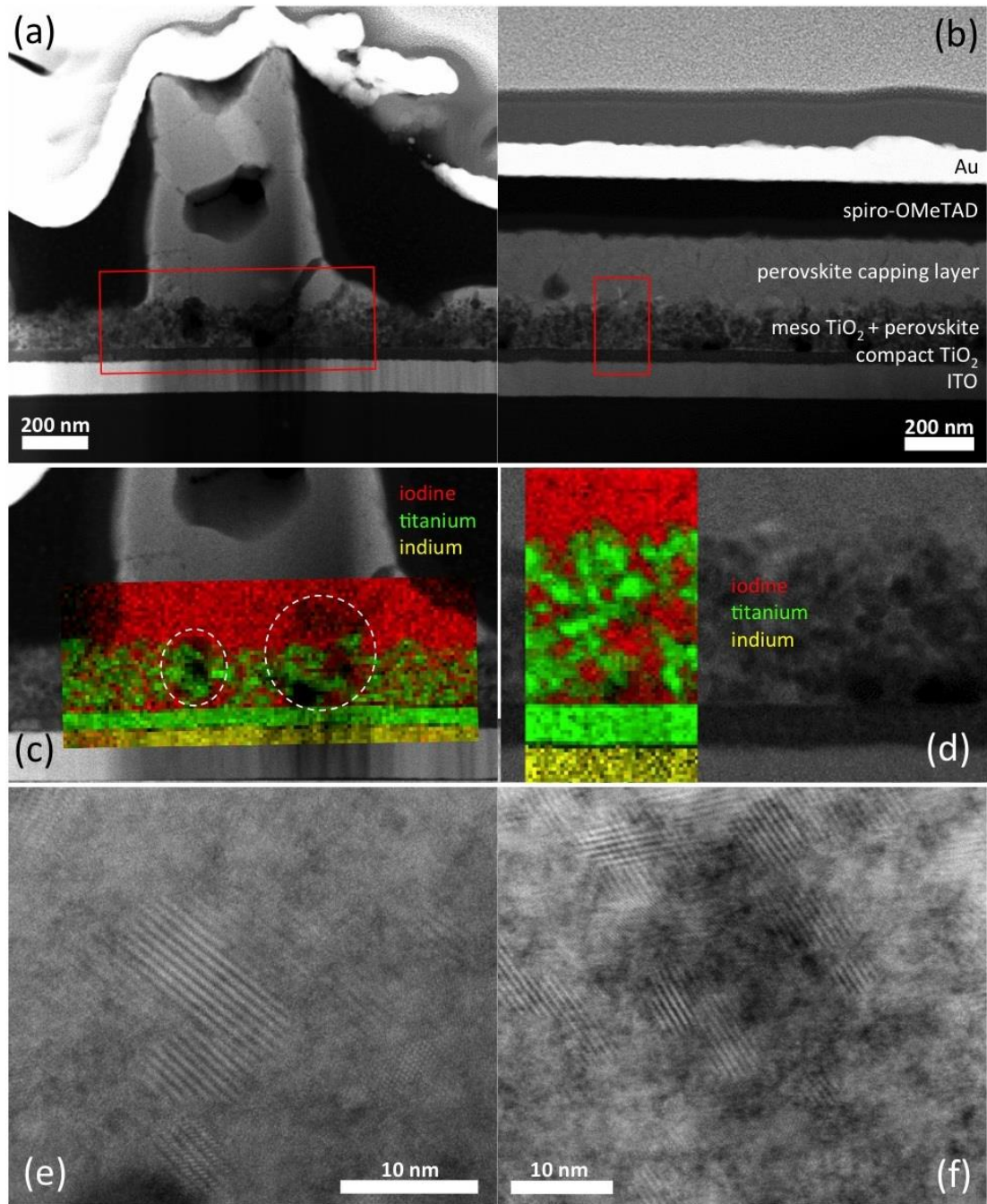
Figure 2: HAADF-STEM cross-sectional image of a complete solar cell with pristine perovskite layer (a) and MA treated perovskite layer (b). The red frames indicate the areas where EELS mapping was performed on samples in (a) and (b), as depicted separately in panel (c) and (d), respectively, with color codes for indium (yellow, M edge), titanium (green, $L_{2,3}$ edge) and iodine (red, $M_{4,5}$ edge), thus representing the ITO, compact + mesoporous TiO_2, and the perovskite. White dashed lines indicate locations with incomplete filling of the mesoporous TiO_2. High magnification images of an area in the bulk of the pristine (e) and MA treated perovskite (f). Lattice fringes can be clearly observed in both cases.

Figure 2a and b show a typical cross-section of a solar cell with a pristine perovskite, and an MA-treated perovskite layer, respectively. The images are aligned with reference to the bottom electrode to facilitate their direct comparison, and the different layers of the device stack are denoted on the right-hand side of Figure 2b. In the pristine case (Figure 2a), a large perovskite structure seems to reside on top of the mesoporous TiO_2, with an ostensible absence of perovskite around it, whereas in the MA treated case a very uniform layer is found, in accordance with the SEM images from Figure 1. What is not clear yet is whether the perovskite is in fact fully infiltrated into the mesoporous matrix, a prerequisite for successful device operation. To this end, we performed Electron Energy Loss Spectroscopy (EELS) on a relevant part of each sample, indicated with a red frame, and show the outcome in a color map in Figure 2c and d. The indium M, titanium $L_{2,3}$ and iodine $M_{4,5}$ edges were extracted and color coded as follows for better visualization of the presence of different elements unique to specific parts of the layer stack: indium (yellow) represents the ITO electrode, titanium (green) corresponds to the compact and mesoporous TiO_2, and iodine (red) identifies the perovskite. With the compact layer of TiO_2 as a well-defined reference below the mesoporous matrix, it can be seen that the latter is fully infiltrated with perovskite in the MA treated sample, whereas there are obvious voids in the region below the large perovskite structure in the pristine sample (indicated with white dashed lines)—which can hamper electron collection. This to some degree confirms the hypothesis of Z. Zhou et al. who suggested that the infiltration of the perovskite precursor would be an issue likely to be mitigated by the MA treatment.[18] Of course there is a possibility that the improvement in device performance in part stems from enhanced interfacial properties, but this will be discussed later on.

As a result of the rough morphology of the pristine perovskite, the spiro-OMeTAD to a large extent follows its topography, resulting locally in very thick regions of Spiro-OMeTAD (>500 nm) and regions with virtually no Spiro-OMeTAD at all. The limited conductivity of this hole transport material undoubtedly induces an undesirable increase in series resistance in the former regions (around 13 $\Omega \cdot cm^2$ on the reverse scan), and inferior carrier selectivity and electron blocking in the latter, which both contribute to a reduced fill factor.

In the MA treated cell, on the contrary, the layer of spiro-OMeTAD atop the perovskite is very uniform and smoothens out the limited roughness still present in the perovskite. With no more than 200 nm, it is sufficiently thin not to compromise the series resistance too much (5-6 $\Omega \cdot cm^2$ on the reverse scan), and allow for a high fill factor (>0.7).

Another interesting observation is the presence of substantial holes in the larger perovskite structures on top of the TiO_2 in the pristine perovskite (Figure 2a). More examples of similar structures found elsewhere in the film are shown in Fig. S2a and b. Their origin most likely lies in the tendency of precipitated PbI_2 nanorods in the precursor solution to eventually grow stacked bundles of perovskite nanorods; this process is particularly prone to defective stacking during the quick evaporation of DMF, resulting in the observed holes.[30-31] Corresponding EELS maps reveal a very distinct carbon K-edge signal

inside the holes (Fig. S2c and d), suggesting that spiro-OMeTAD has infiltrated inside. The resulting alternating layer sequence of perovskite/spiro-OMeTAD/perovskite/Au is unfavorable in terms of energy level alignment, possibly playing a role in the lowered V_{oc} of corresponding devices (see Table 1), and depriving them even more of decent electron blocking capabilities—again affecting the fill factor. If in some cases the holes would not be infiltrated, we surmise the interrupted carrier pathway would lead to a reduced fill factor either way.

The rough morphology and uneven coverage of the pristine perovskite also have consequences for local light absorption, which can at least in part explain the lower J_{sc} for the pristine cells: they contain parts with very thick perovskite capping layer that, given the high absorption coefficient of MAPbI$_3$,[32] absorb 100% of the incoming light, while in other regions—where the capping layer is missing—the perovskite infiltrated in the mesoporous TiO$_2$ (~175 nm) is inadequate for complete light absorption. This must lead to a loss in J_{sc} compared to the MA treated cells, where the uniformly infiltrated perovskite into the mesoporous TiO$_2$ with a capping layer of 250 nm on top does guarantee maximal light absorption. The inferior absorption of pristine films compared to treated ones is confirmed by optical absorption measurements (Fig. S3).

This incomplete perovskite coverage also has other repercussions, as further illustrated by means of AFM data and local current probing via C-AFM. Figure 3a shows the topography image of a pristine sample, and the broad height scale confirms the findings from the cross-sectional HAADF-STEM study, clearly showing the large perovskite structures protruding from the surface. From C-AFM measurements of the same area, and from the resulting current map (Figure 3b), we find that the currents drawn from the regions in between the large perovskite needles are much higher than those drawn from the needles themselves. Local current-voltage measurements (see inset of Figure 3b) show a rectifying behavior that is much more pronounced on the perovskite structures and much less present in the regions in between—with a much steeper curve in the latter case. The MA treated sample exhibits a smoother topography (Figure 3c) and much more uniform current (Figure 3d). Note that the corresponding local IV-curve reveals a very similar rectifying behavior, and that the magnitude of the current measured in this sample is in the order of that corresponding to the perovskite-covered region in the pristine sample. This implies that the currents measured in between the large perovskite structures of the pristine sample are resulting from a direct contact with the mesoporous TiO$_2$ rather than the perovskite (given the lack of capping layer in those regions). This effect is indeed extended to the subsequently deposited Spiro-OMeTAD where clearly a large current is measured in the same regions (see Figure S4). This means that, for a considerable portion of the device area, the —doped— spiro-OMeTAD directly contacts the mesoporous TiO$_2$, which partially shunts the device, degrades the parallel resistance and consequently the fill factor of the device under illumination (as we indeed observe, see Table 1).
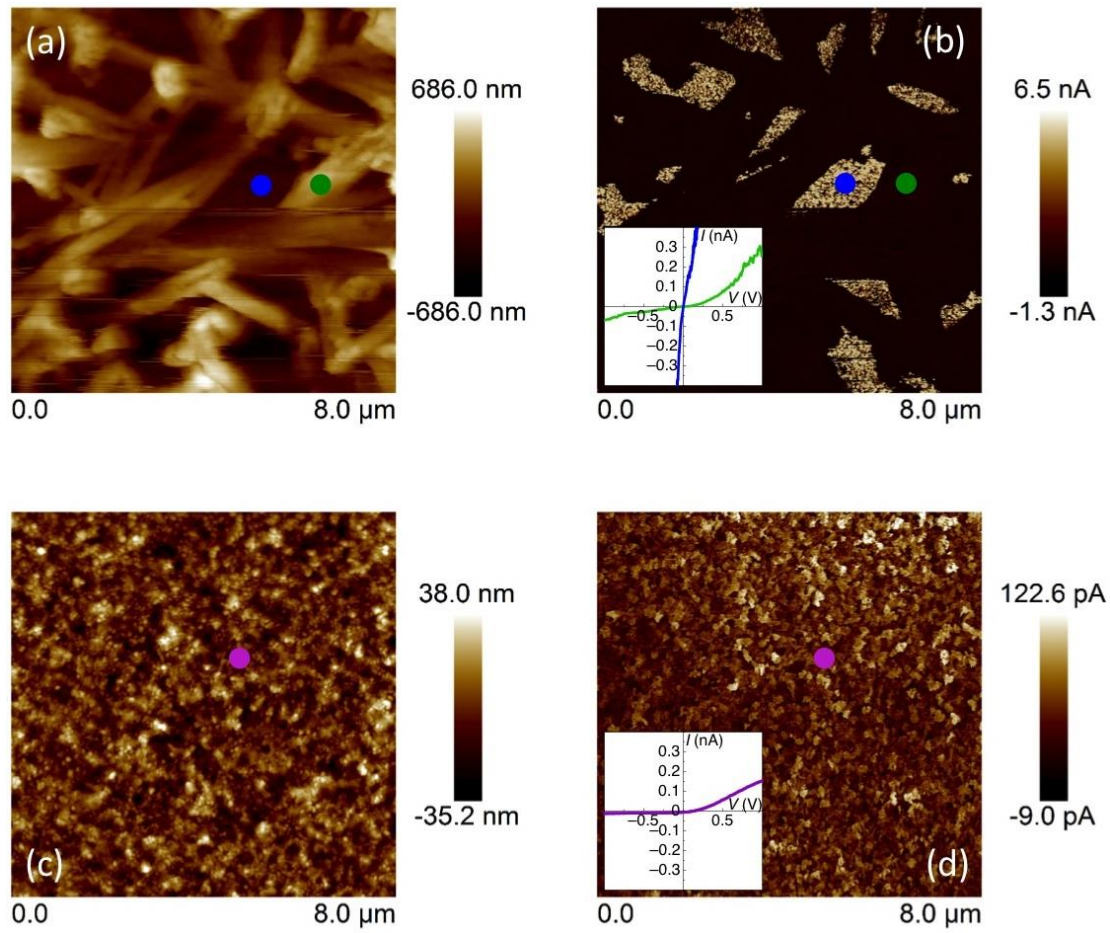
Figure 3: AFM height image (a) and corresponding current map at 0.3V (b) of a pristine mesoporous TiO$_2$/MAPbI$_3$ film; AFM height image (c) and corresponding current map at 0.3V (d) of a MA treated mesoporous TiO$_2$/MAPbI$_3$ film. The insets of (b) and (d) are current-voltage characteristics of specific locations on the films, where the color of the curve corresponds with the location of the marker on the image.

To elucidate the underlying photophysical properties related to the MA treatment, time-resolved photoluminescence (TRPL) measurements were performed on perovskite deposited on mesoporous Al$_2$O$_3$ and TiO$_2$ layers. The use of an insulating and a semiconducting mesoporous scaffold, respectively, with similar thickness and morphology, allows to distinguish observations only related to changes in the morphology on the one hand, and those related to interface effects (carrier injection into the TiO$_2$) on the other hand. Additionally, we performed TRPL measurements with selective excitation from either side (through the capping layer and through the glass and mesoporous oxide layer). This approach allows us to differentiate between the contribution to the PL signal that originates from the perovskite confined in the mesoporous layer and the perovskite capping layer. This is justified considering the absorption depth to be below 100 nm (when exciting with 400 nm), which is less than the thickness of the mesoporous layer and the capping layer.[33-34]

The results of TRPL measurements of the perovskite in the mesoporous layers are shown in Figure 4a and b. The decay kinetics (Figure S5 and Table S1) were fitted with a biexponential function $I(t) = A_1 e^{-t/\tau_1} + A_2 e^{-t/\tau_2} + I_0$ to account for any nonlinearities in the dynamics due to the high initial photon

density ($9.5 \cdot 10^{15} \frac{1}{cm^2}$) required to achieve a reasonable signal-to-noise ratio in these measurements—especially when photoluminescence quenching occurs due to carrier injection into the TiO_2. The initial decay of the charge carrier population at high carrier densities obeys a power law dependence, and upon reaching a density of charge carriers comparable to that of trap states, the carrier recombination dynamics change to exponential. Hence, the bi-exponential fit to the data is rather a parameterization of the entire dynamics and the extracted lifetime τ_1 has no direct physical meaning, while the second decay component described by τ_2 can be assigned to trap-assisted recombination of charge carriers.[35-36] For the insulating Al_2O_3, we observe an increase of the lifetime τ_2 upon MA treatment from 12.7 to 16 ns when the perovskite inside the mesoporous layer is excited. We attribute this to improved pore filling in the mesoporous layer, resulting in larger crystallites.[37] Due to the low signal-to-noise ratio of the measurement, the magnitude of the increase alone would not necessarily provide conclusive evidence thereof, however, the combination of the TRPL with EELS measurements shown in Fig. 2d does very strongly suggest improved pore filling as a result of the treatment.

Performing the same experiment with the perovskite-infiltrated TiO_2, a decrease of the lifetime τ_2 from 10.8 to 8 ns was found upon MA treatment. Assuming that the MA treatment has equally improved pore filling in the TiO_2 mesoporous matrix as before in the Al_2O_3, we attribute this lifetime reduction to more efficient photoluminescence quenching (*ergo* electron-injection into the TiO_2) and, by extension, an indication for improved more intimate interface between the perovskite and the TiO_2. A similar observation was made by Zhao *et al.*, who found improved quenching when using a C_{60} layer instead of mesoporous TiO_2.[25]
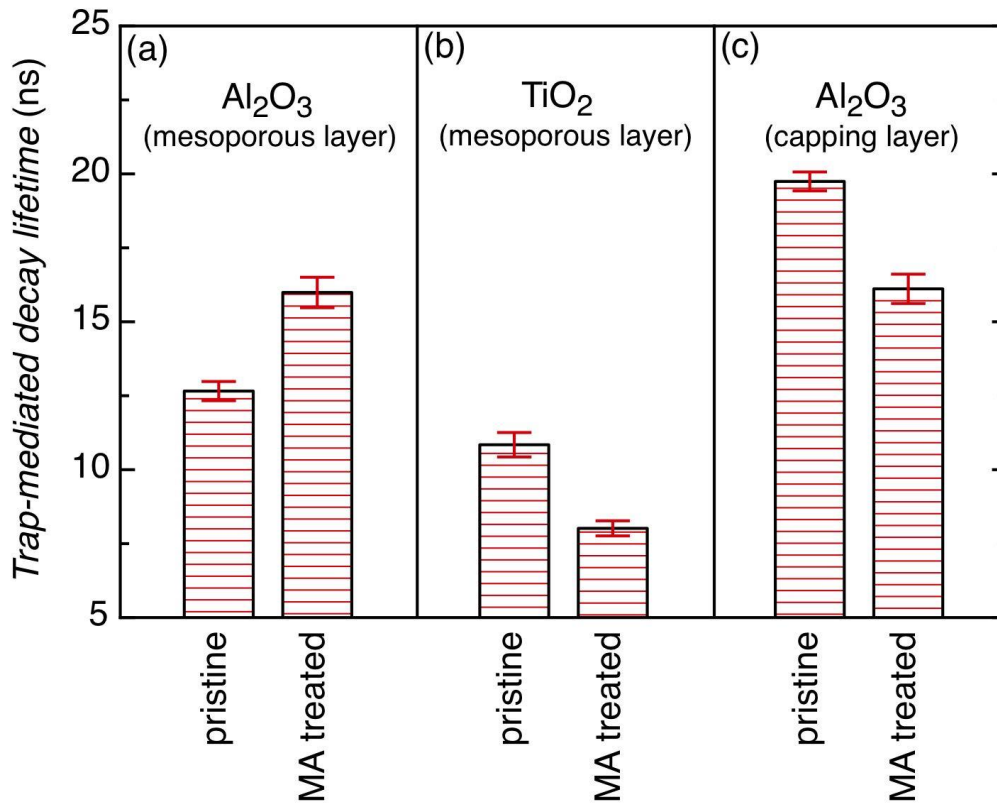
Figure 4: Fitting results of the TRPL measurements performed with a initial photon density of $9.5 \cdot 10^{15}\,cm^{-2}$ at 400 nm: (a) increase of the lifetime due to the MA-treatment from the perovskite confined in a mesoporous layer of Al_2O_3; (b) decrease of the lifetime due to the improved electron-injection after the MA-treatment; (c) decrease of lifetime in the capping layer on top of the Al_2O_3.

We now focus on the size and quality of the perovskite crystallites upon MA treatment. In Figure 1a and b large needle-like morphological features of the pristine sample are manifest, in contrast to the smoother MA treated film (Figure 1c and d). Upon closer inspection of Figure 1b and d it is apparent that the large needles are comprised of crystallites of a size comparable to the crystallites in the smooth film. While the results from SEM and HAADF-STEM suggest a crystallite size of a few hundred nanometers, Debye-Scherrer analysis of the corresponding XRD data (Figure 1e) yields crystallite sizes of around 40 nm for the pristine film, and around 30 nm for the MA treated film. Correspondingly, high magnification HAADF-STEM images reveal lattice fringes (Figure 2e and f) that also delineate domains of a few tens rather than a few hundreds of nanometers. These observations are corroborated by TRPL measurements: in the capping layer a lifetime (τ_2) reduction from 19.7 to 16.1 ns is detected upon MA treatment (Figure 4c), which is consistent with reported findings in case of crystal size reduction.[37] Finally, through optical absorption experiments using Fourier Transform Photocurrent Spectroscopy, the Urbach energy E_U is found to be higher in MA treated films (see Figure S6), which suggests the treatment induces a higher level of disorder.[38] From these results, and together with the morphological study, we infer that the MA treatment induces films of better morphological quality but with inferior electronic quality. This suggests that the significantly better performance of solar cells based on treated films is contingent solely on morphology and improved perovskite/TiO_2

interface, and is conversely tolerant towards deficient electronic quality of the bulk perovskite. Although still somewhat under debate, it does confirm the work of Steirer *et al,* who have shown defects in MAPbI$_3$ need not be active below a certain (prolific) concentration.[39] It is also in line with the recent work of Reid *et al.,* who found that perovskite grains as imaged by SEM are representative of the true electronic domains, and the visible grain boundaries are barriers for transport.[40] Our results add upon this the implication that boundaries between intra-grain features are not detrimental for charge transport.

Conclusion

In summary, MAPbI$_3$ films were fabricated and treated with MA vapor, and solar cells were built based on those films on mesoporous TiO$_2$ scaffolds. Based on a combination of SEM, HAADF-STEM, (C-)AFM and TRPL measurements, we show that the MA treatment facilitates the infiltration of the perovskite into the mesoporous TiO$_2$, indicating improved electron injection into the latter, and evens out the perovskite capping layer to reduce shunting. Contradictorily, it has become apparent that the treatment degenerates the electronic quality of the bulk perovskite, though in light of the vastly improved photovoltaic performance of corresponding solar cells, this effect is heavily subordinate to the enhancement in perovskite morphology and perovskite/TiO$_2$ interface upon treatment. This confirms the defect tolerance of the perovskite on the one hand, and at the same time leaves room for improvement of their crystalline quality in pushing the efficiencies of perovskite solar cells to their theoretical limit.

Methods

Patterned ITO substrates (Jinfung Limited, Xiamen, China) and glass slides were successively cleaned by soap solution, water, acetone, and boiling isopropanol, and underwent a brief oxygen plasma treatment. A titanium precursor solution was prepared by adding a solution of 175μL of Ti isopropoxide in 1.25mL of ethanol into a solution of 17.5μL of 2M HCl (12M diluted by demineralized water) in 1.25 mL of ethanol. This precursor was spin coated at 2000 rpm, and the substrates were then annealed to 500°C for 30 minutes to obtain a compact TiO$_2$ layer. A titania paste (18NR-T, Dyesol) was diluted 1:4 by weight in 1-butanol and spin coated at 4000 rpm on top of the compact TiO$_2$ and calcinated to 500°C for 45 minutes into a mesoporous layer with a thickness of around 175 nm. The perovskite precursor was prepared inside a nitrogen-filled glovebox by dissolving PbI$_2$ and MAI in DMF in a 1:1 molar ratio at 40 wt% and heating at 70°C. The precursor was spin coated inside the glovebox atop the mesoporous layer at 3000 rpm, followed by a thermal treatment at 100°C for 10 minutes. For the samples that required MA treatment, the samples were taken out of the glovebox and into a fumehood. Each sample was held upside down above a 50 ml recipient, filled with 5 ml of MA solution (33% in absolute ethanol, Sigma). A lid was kept on top of the substrate to create a "closed" space where the MA can saturate easier. At the point during exposure where the perovskite completely loses its color (few seconds), the substrate was removed from the MA vapor and horizontally moved above a standard-issue cooling fan

to rapidly recrystallize and remove excess vapor that can cause inhomogeneities in the film. As a second precaution against the retention of remnant traces of MA, the substrate is then kept at 50°C for a few minutes. On all ITO based substrates, a solution of spiro-OMeTAD was spin coated at 3000 rpm (72.3 mg/ml in chlorobenzene with additives of 17.5 μl lithium bis(trifluoromethylsulfonyl) imide (Li-TFSI) (520 mg/ml in acetonitrile) and 28.8 μl 4-butylpyridine). The devices were finished by evaporating a Au electrode at $1 \cdot 10^{-6}$ mbar.

Current-voltage characterization of the solar cells was performed using a solar simulator (Newport 91195A), calibrated with a silicon NIST reference solar cell under AM1.5G conditions at 100 mW/cm². Stabilized power output was measured using a maximum power point tracker built in LabVIEW.

XRD was carried out on a Bruker D8 diffractometer with Cu Kα radiation.

Optical absorption measurements were acquired on an Agilent Cary 5000 UV/Vis-NIR spectrometer.

Fourier transform photocurrent spectroscopy (FTPS) was performed using a Thermo Nicolet 8700 FTIR with an external detector. The spectra were recorded with a quartz beam splitter and appropriate optical band pass filters to improve the signal to noise ratio. All spectra were corrected for the frequency response. Urbach energies were determined by fitting the slope of the spectral tail at low energy.

For the preparation of FIB lamellae, solar cells were prepared in controlled atmosphere as described in our previous work.[41-42] The measurement was performed using a vacuum transfer holder inside a FEI Titan 60-300 microscope equipped with an X-FEG high brightness electron source, a probe Cs corrector, a Super-X 4-quadrant EDX detector and a Gatan GIF Enfinium electron energy loss (EELS) spectrometer. The microscope was operated at 200 kV in Scanning TEM mode with a low electron dose to avoid electron-induced damage to the perovskite. Imaging was performed with a 21 mrad convergence angle and collection of all electrons in the range 46–160 mrad for high angle annular dark field (HAADF). EELS measurements were performed with a beam current of ≈50 pA.

Atomic Force Microscopy analysis was performed with a Bruker Multimode 8, mounting the PeakForce TUNA application module and operated in contact mode. The used probes were coated with Pt/Ir and had a nominal spring constant of 0.4N/m.

Time-resolved photoluminescence was measured with a C5680 Hamamatsu streak camera system following excitation at 400 nm from a frequency-doubled mode-locked Ti:Sa system (Coherent Libra) with a pulse with of 100 fs, a repetition rate of 1 kHz and an initial photon density of $9.5 \cdot 10^{15} \frac{1}{cm^2}$ (1μJ/cm²). The samples were excited under vacuum (p < 10^{-5} mbar) through the substrate and face-on.

Associated content

Supporting Information

The Supporting Information is available free of charge on the ACS Publications website.

The JV-curves and SPO curves of champion pristine and MA treated devices; additional cross-sectional HAADF-STEM images of pristine devices, together with EELS analysis of voids in the perovskite; optical absorption spectra of pristine and MA treated perovskite films; C-AFM measurements of spiro-OMeTAD coated pristine and MA treated perovskite films; PL measurements and fitting parameters used to determine the time constants in Figure 4; Urbach energies for pristine and MA treated perovskite films.

Author information

Corresponding author:

* E-mail: bert.conings@uhasselt.be

Notes:

The authors declare no competing fin   ancial interest

Acknowledgements

References

(1)   Lin, Q.; Armin, A.; Burn, P. L.; Meredith, P. Organohalide Perovskites for Solar Energy Conversion. *Acc. Chem. Res.* **2016**, *49*, 545-553.

(2)   Tong, X.; Lin, F.; Wu, J.; Wang, Z. M. High Performance Perovskite Solar Cells. *Adv. Sci* **2015**, *3*, 1500201.

(3)   Zuo, C.; Bolink, H. J.; Han, H.; Huang, J.; Cahen, D.; Ding, L. Advances in Perovskite Solar Cells. *Adv. Sci* **2016**, *3*, 1500324.

(4)   Barrows, A. T.; Pearson, A. J.; Kwak, C. K.; Dunbar, A. D. F.; Buckley, A. R.; Lidzey, D. G. Efficient Planar Heterojunction Mixed-Halide Perovskite Solar Cells Deposited Via Spray-Deposition. *Energy Environ. Sci.* **2014**, *7*, 2944-2950.

(5)   Hwang, K.; Jung, Y.-S.; Heo, Y.-J.; Scholes, F. H.; Watkins, S. E.; Subbiah, J.; Jones, D. J.; Kim, D.-Y.; Vak, D. Toward Large Scale Roll-to-Roll Production of Fully Printed Perovskite Solar Cells. *Adv. Mater.* **2015**, *27*, 1241-1247.

(6)   Yang, Z.; Chueh, C.-C.; Zuo, F.; Kim, J. H.; Liang, P.-W.; Jen, A. K. Y. High-Performance Fully Printable Perovskite Solar Cells Via Blade-Coating Technique under the Ambient Condition. *Adv. Energy Mater.* **2015**, *5*, 1500328.

(7)   Zhang, H.; Mao, J.; He, H.; Zhang, D.; Zhu, H. L.; Xie, F.; Wong, K. S.; Grätzel, M.; Choy, W. C. H. A Smooth Ch3nh3pbi3 Film Via a New Approach for Forming the PbI2 Nanostructure Together with

Strategically High CH3NH3I Concentration for High Efficient Planar-Heterojunction Solar Cells. *Adv. Energy Mater.* **2015**, *5*, n/a-n/a.

(8)   Chang, J.; Lin, Z.; Zhu, H.; Isikgor, F. H.; Xu, Q.-H.; Zhang, C.; Hao, Y.; Ouyang, J. Enhancing the Photovoltaic Performance of Planar Heterojunction Perovskite Solar Cells by Doping the Perovskite Layer with Alkali Metal Ions. *J. Mater. Chem. A* **2016**, *4*, 16546-16552.

(9)   Hsu, H.-L.; Chen, C.-P.; Chang, J.-Y.; Yu, Y.-Y.; Shen, Y.-K. Two-Step Thermal Annealing Improves the Morphology of Spin-Coated Films for Highly Efficient Perovskite Hybrid Photovoltaics. *Nanoscale* **2014**, *6*, 10281-10288.

(10)   Xie, F. X.; Zhang, D.; Su, H.; Ren, X.; Wong, K. S.; Grätzel, M.; Choy, W. C. H. Vacuum-Assisted Thermal Annealing of CH3NH3PbI3 for Highly Stable and Efficient Perovskite Solar Cells. *ACS Nano* **2015**, *9*, 639-646.

(11)   Sun, X., et al. Mixed-Solvent-Vapor Annealing of Perovskite for Photovoltaic Device Efficiency Enhancement. *Nano Energy* **2016**, *28*, 417-425.

(12)   Xiao, Z.; Dong, Q.; Bi, C.; Shao, Y.; Yuan, Y.; Huang, J. Solvent Annealing of Perovskite-Induced Crystal Growth for Photovoltaic-Device Efficiency Enhancement. *Adv. Mater.* **2014**, *26*, 6503-6509.

(13)   Liu, D.; Wu, L.; Li, C.; Ren, S.; Zhang, J.; Li, W.; Feng, L. Controlling CH3NH3PbI3–Xclx Film Morphology with Two-Step Annealing Method for Efficient Hybrid Perovskite Solar Cells. *ACS Appl. Mater. Interfaces* **2015**, *7*, 16330-16337.

(14)   Eperon, G. E., et al. The Importance of Moisture in Hybrid Lead Halide Perovskite Thin Film Fabrication. *ACS Nano* **2015**, *9*, 9380-9393.

(15)   Dong, Q.; Yuan, Y.; Shao, Y.; Fang, Y.; Wang, Q.; Huang, J. Abnormal Crystal Growth in Ch3nh3pbi3-Xclx Using a Multi-Cycle Solution Coating Process. *Energy Environ. Sci.* **2015**, *8*, 2464-2470.

(16)   Yang, M.; Zhang, T.; Schulz, P.; Li, Z.; Li, G.; Kim, D. H.; Guo, N.; Berry, J. J.; Zhu, K.; Zhao, Y. Facile Fabrication of Large-Grain Ch3nh3pbi3–Xbrx Films for High-Efficiency Solar Cells Via CH3NH3Br-Selective Ostwald Ripening. *Nat. Commun.* **2016**, *7*, 12305.

(17)   Zhu, W.; Bao, C.; Wang, Y.; Li, F.; Zhou, X.; Yang, J.; Lv, B.; Wang, X.; Yu, T.; Zou, Z. Coarsening of One-Step Deposited Organolead Triiodide Perovskite Films Via Ostwald Ripening for High Efficiency Planar-Heterojunction Solar Cells. *Dalton Trans.* **2016**, *45*, 7856-7865.

(18)   Zhou, Z.; Wang, Z.; Zhou, Y.; Pang, S.; Wang, D.; Xu, H.; Liu, Z.; Padture, N. P.; Cui, G. Methylamine-Gas-Induced Defect-Healing Behavior of Ch3nh3pbi3 Thin Films for Perovskite Solar Cells. *Angew. Chem., Int. Ed.* **2015**, *54*, 9705-9709.

(19)   Zhou, Y.; Yang, M.; Pang, S.; Zhu, K.; Padture, N. P. Exceptional Morphology-Preserving Evolution of Formamidinium Lead Triiodide Perovskite Thin Films Via Organic-Cation Displacement. *J. Am. Chem. Soc.* **2016**, *138*, 5535-5538.

(20)   Momblona, C.; Gil-Escrig, L.; Bandiello, E.; Hutter, E. M.; Sessolo, M.; Lederer, K.; Blochwitz-Nimoth, J.; Bolink, H. J. Efficient Vacuum Deposited P-I-N and N-I-P Perovskite Solar Cells Employing Doped Charge Transport Layers. *Energy Environ. Sci.* **2016**, *9*, 3456-3463.

(21)   Liu, M.; Johnston, M. B.; Snaith, H. J. Efficient Planar Heterojunction Perovskite Solar Cells by Vapour Deposition. *Nature* **2013**, *501*, 395-398.

(22)   Raga, S. R.; Ono, L. K.; Qi, Y. Rapid Perovskite Formation by Ch3nh2 Gas-Induced Intercalation and Reaction of Pbi2. *J. Mater. Chem. A* **2016**, *4*, 2494-2500.

(23)   Jacobs, D. L.; Zang, L. Thermally Induced Recrystallization of Mapbi3 Perovskite under Methylamine Atmosphere: An Approach to Fabricating Large Uniform Crystalline Grains. *Chem. Commun.* **2016**, *52*, 10743-10746.

(24)   Jiang, Y.; Juarez-Perez, E. J.; Ge, Q.; Wang, S.; Leyden, M. R.; Ono, L. K.; Raga, S. R.; Hu, J.; Qi, Y. Post-Annealing of MAPbI3 Perovskite Films with Methylamine for Efficient Perovskite Solar Cells. *Mater. Horiz.* **2016**, *3*, 548-555.

(25)   Zhao, T.; Williams, S. T.; Chueh, C.-C.; deQuilettes, D. W.; Liang, P.-W.; Ginger, D. S.; Jen, A. K. Y. Design Rules for the Broad Application of Fast (<1 S) Methylamine Vapor Based, Hybrid Perovskite Post Deposition Treatments. *RSC Adv.* **2016**, *6*, 27475-27484.

(26)   Wang, Q.; Shao, Y.; Dong, Q.; Xiao, Z.; Yuan, Y.; Huang, J. Large Fill-Factor Bilayer Iodine Perovskite Solar Cells Fabricated by a Low-Temperature Solution-Process. *Energy Environ. Sci.* **2014**, *7*, 2359-2365.

(27)   Zhao, Y.; Zhu, K. Ch3nh3cl-Assisted One-Step Solution Growth of Ch3nh3pbi3: Structure, Charge-Carrier Dynamics, and Photovoltaic Properties of Perovskite Solar Cells. *J. Phys. Chem. C.* **2014**, *118*, 9412-9418.

(28)   Snaith, H. J.; Abate, A.; Ball, J. M.; Eperon, G. E.; Leijtens, T.; Noel, N. K.; Stranks, S. D.; Wang, J. T.-W.; Wojciechowski, K.; Zhang, W. Anomalous Hysteresis in Perovskite Solar Cells. *J. Phys. Chem. Lett.* **2014**, *5*, 1511-1515.

(29)   Unger, E. L.; Hoke, E. T.; Bailie, C. D.; Nguyen, W. H.; Bowring, A. R.; Heumuller, T.; Christoforo, M. G.; McGehee, M. D. Hysteresis and Transient Behavior in Current-Voltage Measurements of Hybrid-Perovskite Absorber Solar Cells. *Energy Environ. Sci.* **2014**, *7*, 3690-3698.

(30)   Ahn, N.; Son, D.-Y.; Jang, I.-H.; Kang, S. M.; Choi, M.; Park, N.-G. Highly Reproducible Perovskite Solar Cells with Average Efficiency of 18.3% and Best Efficiency of 19.7% Fabricated Via Lewis Base Adduct of Lead(II) Iodide. *J. Am. Chem. Soc.* **2015**, *137*, 8696-8699.

(31)   Yan, K.; Long, M.; Zhang, T.; Wei, Z.; Chen, H.; Yang, S.; Xu, J. Hybrid Halide Perovskite Solar Cell Precursors: Colloidal Chemistry and Coordination Engineering Behind Device Processing for High Efficiency. *J. Am. Chem. Soc.* **2015**, *137*, 4460-4468.

(32)   Green, M. A.; Jiang, Y.; Soufiani, A. M.; Ho-Baillie, A. Optical Properties of Photovoltaic Organic–Inorganic Lead Halide Perovskites. *J. Phys. Chem. Lett.* **2015**, *6*, 4774-4785.

(33)   Grancini, G.; Srimath Kandada, A. R.; Frost, J. M.; Barker, A. J.; De Bastiani, M.; Gandini, M.; Marras, S.; Lanzani, G.; Walsh, A.; Petrozza, A. Role of Microstructure in the Electron–Hole Interaction of Hybrid Lead Halide Perovskites. *Nat. Photonics* **2015**, *9*, 695-701.

(34)   Mosconi, E.; Grancini, G.; Roldán-Carmona, C.; Gratia, P.; Zimmermann, I.; Nazeeruddin, M. K.; De Angelis, F. Enhanced TiO2/MAPbI3 Electronic Coupling by Interface Modification with Pbi2. *Chem. Mater.* **2016**, *28*, 3612-3615.

(35)   Stranks, S. D.; Burlakov, V. M.; Leijtens, T.; Ball, J. M.; Goriely, A.; Snaith, H. J. Recombination Kinetics in Organic-Inorganic Perovskites: Excitons, Free Charge, and Subgap States. *Phys. Rev. Appl.* **2014**, *2*, 034007.

(36)   Manser, J. S.; Kamat, P. V. Band Filling with Free Charge Carriers in Organometal Halide Perovskites. *Nat. Photonics* **2014**, *8*, 737-743.

(37)   D'Innocenzo, V.; Srimath Kandada, A. R.; De Bastiani, M.; Gandini, M.; Petrozza, A. Tuning the Light Emission Properties by Band Gap Engineering in Hybrid Lead Halide Perovskite. *J. Am. Chem. Soc.* **2014**, *136*, 17730-17733.

(38)   De Wolf, S.; Holovsky, J.; Moon, S.-J.; Löper, P.; Niesen, B.; Ledinsky, M.; Haug, F.-J.; Yum, J.-H.; Ballif, C. Organometallic Halide Perovskites: Sharp Optical Absorption Edge and Its Relation to Photovoltaic Performance. *J. Phys. Chem. Lett.* **2014**, *5*, 1035-1039.

(39)   Steirer, K. X.; Schulz, P.; Teeter, G.; Stevanovic, V.; Yang, M.; Zhu, K.; Berry, J. J. Defect Tolerance in Methylammonium Lead Triiodide Perovskite. *ACS Energy. Lett.* **2016**, *1*, 360-366.

(40)   Reid, O. G.; Yang, M.; Kopidakis, N.; Zhu, K.; Rumbles, G. Grain-Size-Limited Mobility in Methylammonium Lead Iodide Perovskite Thin Films. *ACS Energy. Lett.* **2016**, *1*, 561-565.

(41)   Conings, B., et al. Intrinsic Thermal Instability of Methylammonium Lead Trihalide Perovskite. *Adv. Energy Mater.* **2015**, *5*, 201500477.

(42)   Conings, B.; Babayigit, A.; Klug, M. T.; Bai, S.; Gauquelin, N.; Sakai, N.; Wang, J. T.-W.; Verbeeck, J.; Boyen, H.-G.; Snaith, H. J. A Universal Deposition Protocol for Planar Heterojunction Solar Cells with High Efficiency Based on Hybrid Lead Halide Perovskite Families. *Adv. Mater.* **2016**, *28*, 10701-10709.

Supporting Information

Structure-Property Relations of Methylamine Vapor Treated Hybrid Perovskite CH₃NH₃PbI₃ Films and Solar Cells

Bert Conings[1,2]*, Simon A. Bretschneider[3], Aslihan Babayigit[1,2], Nicolas Gauquelin[4], Ilaria Cardinaletti[1], Jean Manca[5], Jo Verbeeck[4], Henry J. Snaith[2], Hans-Gerd Boyen[1]

[1]Hasselt University, Institute for Materials Research (IMO), Wetenschapspark 1, 3590 Diepenbeek, Belgium.

[2]University of Oxford, Department of Physics, Clarendon Laboratory, Parks Road, Oxford OX1 3PU, UK.

[3]Max Planck Institute for Polymer Research - Molecular Spectroscopy Group, Ackermannweg 10, 55128 Mainz, Germany.

[4]University of Antwerp, Electron Microscopy for Materials Research, University of Antwerp, Groenenborgerlaan 171, 2020, Antwerp, Belgium.

[5]Hasselt University, X-Lab, Agoralaan 1, Building D, 3590, Diepenbeek, Belgium.
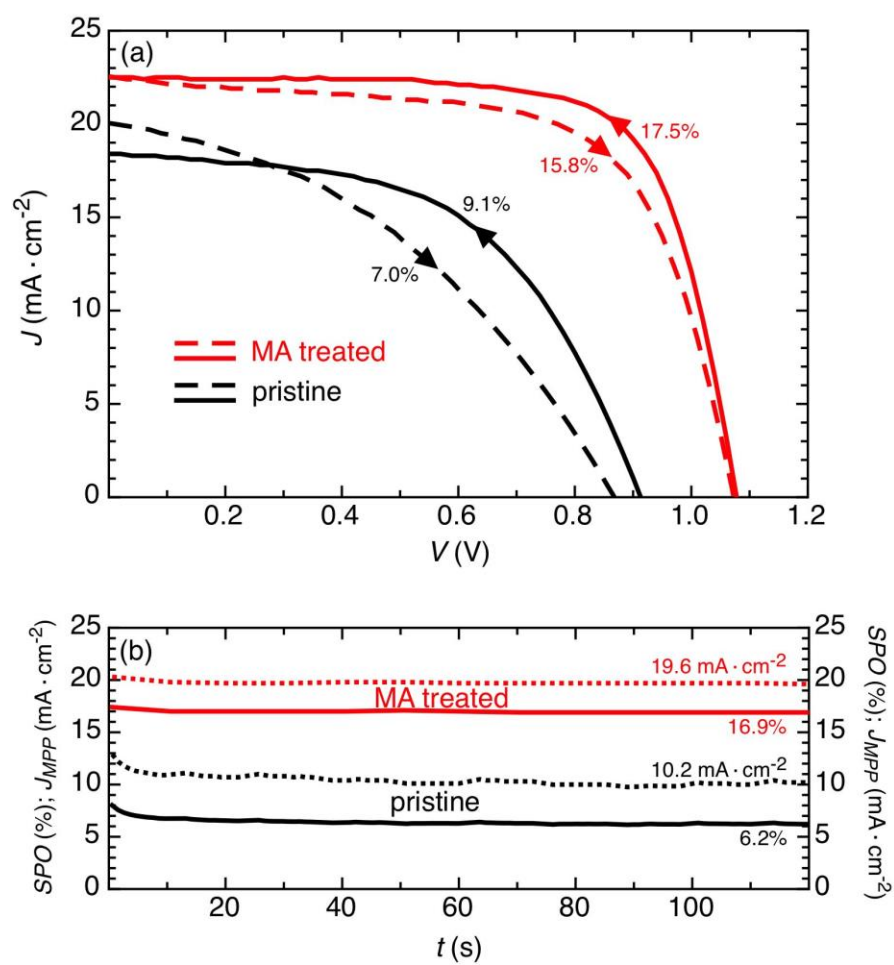
*bert.conings@uhasselt.be

Figure S1: (a) Forward and reverse JV-scans of the champion devices; (b) SPO and current density at maximum power point for the same devices.
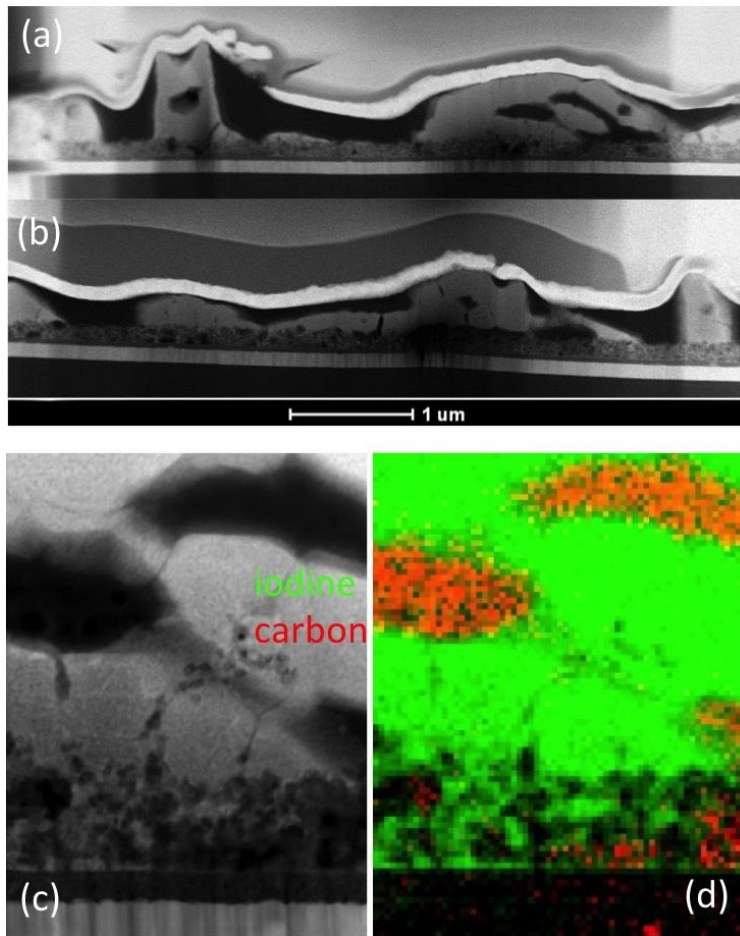
Figure S2: (a) and (b): additional HAADF-STEM cross-sections of solar cells based on pristine perovskite layers. (c) Region with holes inside large perovskite structures and (d) corresponding EELS map, indicating a large carbon signal inside those holes.
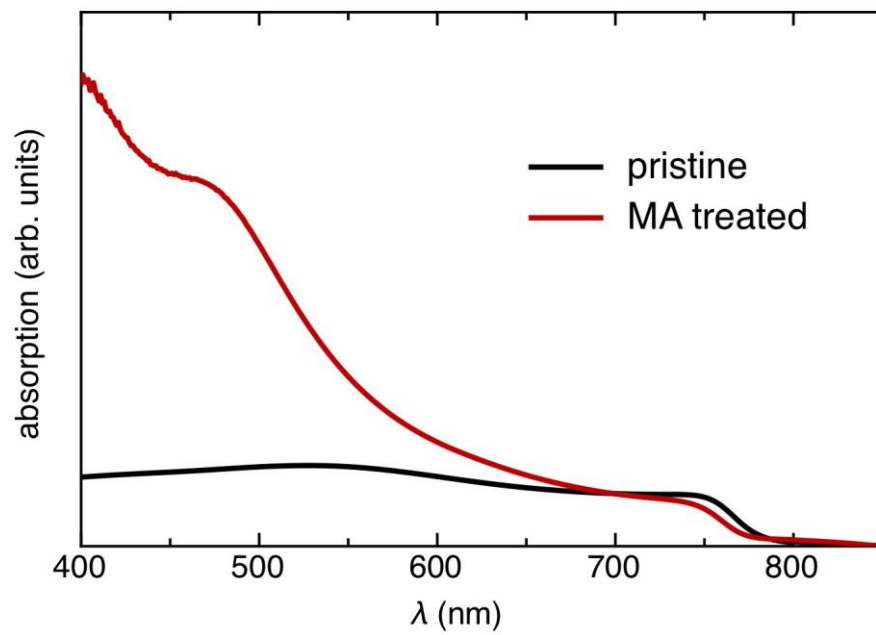
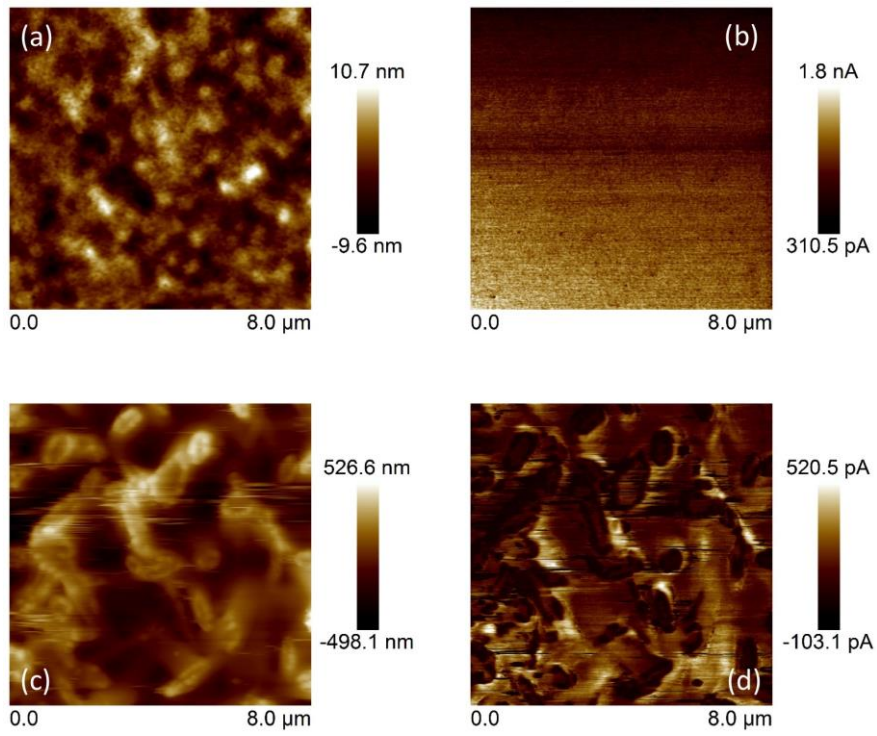Figure S3: Optical absorption spectra of a pristine and a MA treated MAPbI$_3$ film on glass.

Figure S4: AFM height image (a) and corresponding current map at 0.3V (b) of an MA treated mesoTiO$_2$/MAPbI$_3$ film with Spiro-OMeTAD on top; AFM image (c) and corresponding C-AFM image at 0.3V (d) of a pristine mesoTiO$_2$/MAPbI$_3$ film with Spiro-OMeTAD on top.
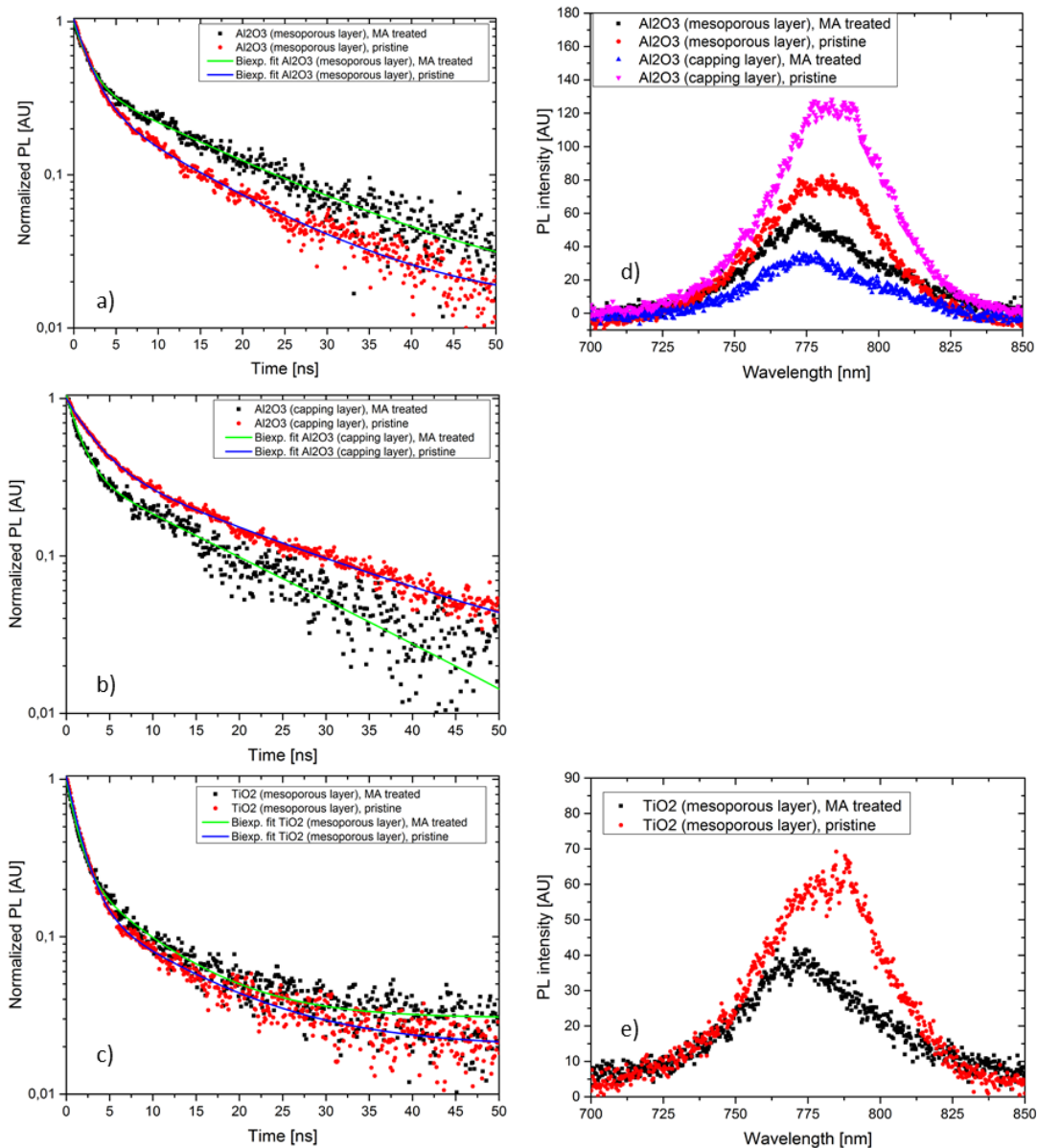
Figure S5: TRPL measurements of pristine and MA treated samples. (a) Kinetics of the perovskite in the mesoporous Al_2O_3; (b) Kinetics of the perovskite in the capping layer on top of the mesoporous Al_2O_3; (c) Kinetics of the perovskite confined in the mesoporous TiO_2. (d) Spectra of the perovskite for the Al_2O_3; (e) Spectra of the perovskite confined in the mesoporous TiO_2.

We chose a normalized chart of the photoluminescence decay data in order to allow better comparability of the traces. As shown in Fig. S5 (d), the photoluminescence intensity of the treated samples is generally lower, thus a larger apparent noise can be seen in the normalized decay traces. Due to the lower overall PL intensity for the perovskite confined in the mesoporous TiO_2., the noise level is higher compared to the measurement for Al_2O_3.
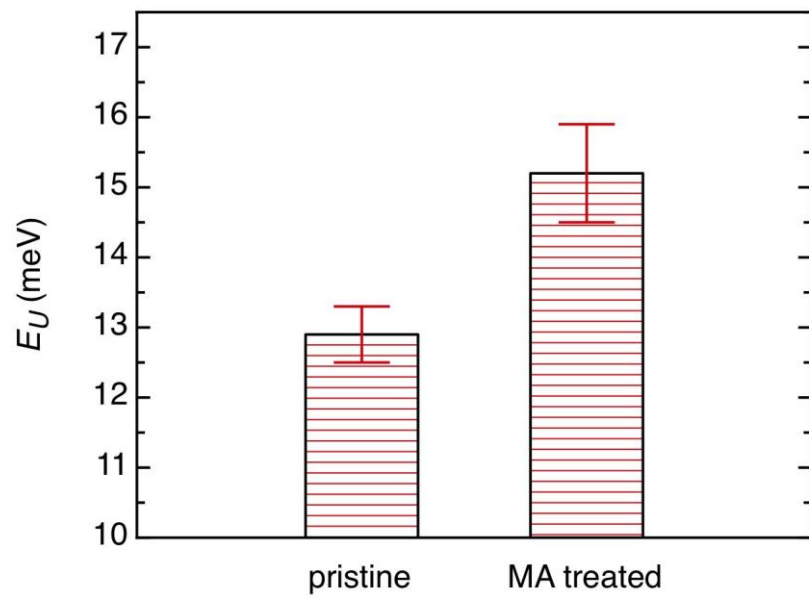
Figure S6: Urbach energy for pristine and MA treated perovskite.

Table S1: Fitting parameters for the TRPL measurements.

		Al_2O_3 (mesoporous)	Al_2O_3 (capping)	TiO_2 (mesoporous)
MA treated	I_0	0,015±0,003	0,001±0,002	0,030±0,001
	A_1	0,598±0,008	0,711±0,010	0,728±0,008
	τ_1	1,613±0,043	1,600±0,044	1,206±0,024
	A_2	0,382±0,005	0,345±0,007	0,239±0,007
	τ_2	15,991±0,515	16,114±0,496	8,017±0,255
pristine	I_0	0,013±0,001	0,014±0,001	0,020±0,001
	A_1	0,726±0,006	0,609±0,005	0,871±0,005
	τ_1	1,919±0,028	3,065±0,043	1,519±0,016
	A_2	0,295±0,005	0,380±0,005	0,151±0,004
	τ_2	12,657±0,324	19,745±0,320	10,843±0,413